OPEN ACCESS
IOP Publishing
Journal of Physics D: Applied Physics
J. Phys. D: Appl. Phys. **50** (2017) 415202 (13pp)
https://doi.org/10.1088/1361-6463/aa875a

Spatio-temporal characterization of the multiple current pulse regime of diffuse barrier discharges in helium with nitrogen admixtures

Marc Bogaczyk[1], Robert Tschiersch[2], Sebastian Nemschokmichal[2,3] and Jürgen Meichsner[2]

[1] Leibniz Institute for Plasma Science and Technology (INP Greifswald), Felix-Hausdorff-Str. 2, 17489 Greifswald, Germany
[2] Institute of Physics, University of Greifswald, Felix-Hausdorff-Str. 6, 17489 Greifswald, Germany

E-mail: nemschok@physik.uni-greifswald.de

Received 31 May 2017, revised 7 August 2017
Accepted for publication 21 August 2017
Published 20 September 2017

Abstract

This work reports on the spatio-temporal characterization of the multiple current pulse regime of diffuse barrier discharges driven by sine-wave feeding voltage at a frequency of 2 kHz in helium with small nitrogen admixtures. The discharge gap of 3 mm is bounded by glass plates on both plane electrodes. Priority is given to the lateral discharge inhomogeneities, underlying volume- and surface-memory effects, and the breakdown mechanism. Therefore, relevant processes in the discharge volume and on the dielectric surfaces were investigated by ICCD camera imaging and optical emission spectroscopy in combination with electrical measurements and surface charge diagnostics using the electro-optic Pockels effect of a bismuth silicon oxide crystal. The number of current pulses per half-cycle of the sine-wave voltage rises with increasing nitrogen admixture to helium due to the predominant role of the Penning ionization. Here, the transition from the first glow-like breakdown to the last Townsend-like breakdown is favored by residual species from the former breakdowns which enhance the secondary electron emission during the pre-phase of the later breakdowns. Moreover, the surface charge measurements reveal that the consecutive breakdowns occur alternately at central and peripheral regions on the electrode surface. These spatial inhomogeneities are conserved by the surface charge memory effect as pointed out by the recalculated spatio-temporal development of the gap voltage.

Keywords: barrier discharge, multiple current pulses, existence regimes, breakdown mechanism, surface charge, gap voltage, memory effect

(Some figures may appear in colour only in the online journal)

[3] Author to whom any correspondence should be addressed.

1. Introduction

The possibility to generate non-equilibrium plasmas at atmospheric pressure with comparatively low power consumptions make the barrier discharge (BD) indispensable for numerous industrial applications [1–4]. During the breakdown, the charge carriers from the discharge volume accumulate onto the dielectric barrier covering the electrodes. These surface charges cause an electric field across the gas gap that is oppositely directed to the electric field by the applied voltage, which finally results in the discharge extinction. Thereby, the transition to arc discharges is avoided. That is why BD-based applications such as the surface treatment of heat-sensitive samples in biology, life-science, and medicine benefit from the compromise of high chemical reactivity at low gas temperature [5–8].

Different discharge phenomena appear depending on the gas composition, pressure, and flow, as well as on the electrode configuration, dielectric material, and feeding voltage amplitude and shape. The well-known microdischarge regime is characterized by multiple arbitrary distributed breakdowns on the nanosecond time scale, and typically operated in oxygen-containing gas mixtures [9–13]. In contrast, the glow-like and Townsend-like BDs in pure helium and pure nitrogen usually appear laterally diffuse, and operate on the microsecond time scale [14–19]. The differing breakdown mechanisms are mainly determined by the ratio between the volume ionization and the secondary electron emission, the pre-ionization by metastable species, and the presence or absence of local space charge formation resulting in the distortion of the electric field across the discharge gap. Note that these different discharge modes can be observed within a close range of operating conditions [20–24].

The transition regime between the common laterally diffuse and filamentary discharge modes is often characterized by several stationary current pulses per half-period of the feeding voltage. This multiple current pulse regime of the diffuse discharge is typical for the operation in binary gas mixtures, including helium and nitrogen or oxygen [25–31]. Spatio-temporally resolved current measurements using segmented electrodes in case of such a discharge with several stationary current pulses per half-period revealed that the consecutive breakdowns occur in different radially symmetric regions [26]. Such an effect was not yet measured by surface charge diagnostics based on the electro-optic Pockels effect of a bismuth silicon oxide crystal. But, previous studies of the multiple current pulse regime in helium revealed a discrepancy between the total transported charge and deposited surface charge [32]. This discrepancy is probably caused by discharge breakdowns in different radial positions outside the limited centered observation window. The latter accounts only for the surface charge in the central part of the discharge configuration. To address this issue, the observation area of the surface charge measurement was extended. Furthermore, the surface charge measurement is complemented by optical emission spectroscopy and ICCD camera imaging to clarify the breakdown mechanisms of the consecutive current pulses, as well as the role of volume- and surface-memory effects for these breakdown mechanisms and the lateral discharge structure. Overall, a better knowledge about the multiple current pulse regime will provide a better insight into the transition between laterally diffuse and filamentary discharges.

The outline of the article is as follows. Section 2 briefly describes the experimental setup and the diagnostic techniques used. In section 3, the electrical characteristics and parameter dependencies of the multiple current pulse regime are presented. The breakdown mechanisms and underlying volume-memory effects are discussed in section 4. Finally, the lateral discharge development and the importance of the surface charge memory effect are highlighted in section 5.

2. Experimental setup

2.1. Discharge configuration and gas supply

The plane-parallel discharge configuration with a discharge gap distance of 3 mm is depicted in figure 1. The high-voltage driven electrode is a copper ring connected to an electrically conductive and optically transparent ITO layer coated on a float glass plate. This allows the observation of the discharge from above. On top of the grounded aluminum mirror, a bismuth silicon oxide (BSO) crystal is mounted and covered with a thin borosilicate glass plate. The electro-optic BSO crystal enables the measurement of surface charges deposited on the borosilicate glass during the discharge operation. The respective relative permittivities and thicknesses of the dielectric materials are summarized in table 1. Before the discharge operation, the vacuum chamber enclosing the discharge configuration was evacuated to a base pressure below 10^{-5} mbar. Two mass flow controllers set the gas flow rate (100 sccm) of helium and nitrogen (respective purity $> 99.999\%$), whereby well-defined He/N_2 mixtures flow directly into the discharge volume. The operating pressure of 500 mbar was kept constant in the flowing regime by a diaphragm pressure gauge (MKS) in combination with a butterfly valve (MKS) and a process pump (TRIVAC D25BCSPFPE).

2.2. Electrical supply and measurements

Figure 2 illustrates the experimental setup which enables the investigation of electrical discharge characteristics (a), the distribution and dynamics of surface charges (b), and the discharge development in the volume (c,d) under identical operating conditions.

The sine-wave feeding voltage $U_{ext}(t)$ at the frequency of 2 kHz is provided by a function generator (SRS DS345) in combination with an amplifier (Trek 615-10), measured by a voltage probe, and connected to the upper electrode. Moreover, the total transported charge $Q_{ext}(t)$ was detected using an external capacitor ($C_{ext} = 1.2$ nF). Data acquisition and processing was performed using a digital oscilloscope (ROHDE&SCHWARZ RTO1024) and a conventional PC.

For the calculation of the internal electrical quantities such as the gap voltage and the discharge current, an electrical equivalent circuit is necessary. Since the diameter of the electrodes are different, two equivalent circuit diagrams

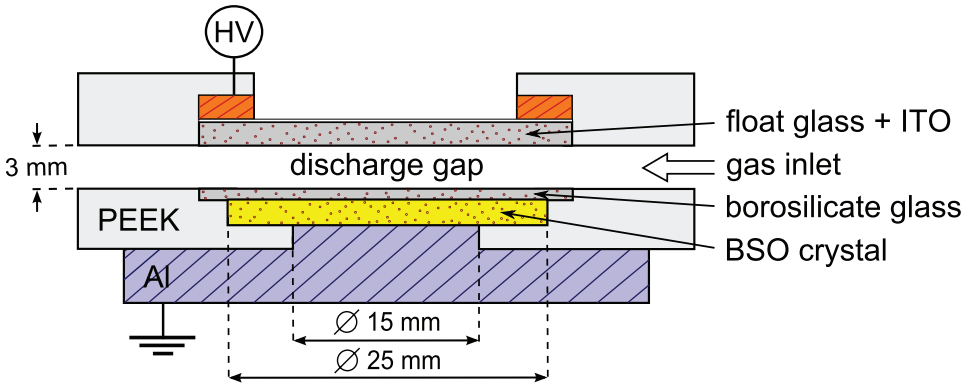

Figure 1. Sketch of the discharge configuration (side view).

Table 1. Relative permittivities and thicknesses of the dielectrics and the gas gap.

Material i	Relative permittivity ε_i	Thickness d_i/mm
Gap	1	3
Glass1	7.6	0.7
Glass2	6.7	0.2
BSO	56	0.7
PEEK	3.2	4

are considered (figure 3). The first equivalent circuit diagram in figure 3(a) assumes that the discharge diameter is limited by the smaller bottom electrode with a radius $R_1 = 7.5$ mm. Under this assumption, the capacitance of the dielectrics $C^{\bullet}_{\mathrm{diel}}$ is calculated as a series of the capacitances $C^{\bullet}_{\mathrm{glass1}}$, $C^{\bullet}_{\mathrm{glass2}}$, and $C^{\bullet}_{\mathrm{BSO}}$, each calculated by $C^{\bullet}_i = \varepsilon_i\varepsilon_0\pi R_1^2/d_i$ including the electric field constant ε_0, the relative permittivities ε_i and the thicknesses d_i of the dielectrics (table 1). In the second equivalent circuit diagram in figure 3(b), the ring-shaped area between the radius $R_1 = 7.5$ mm of the bottom electrode and the radius $R_2 = 12.5$ mm of the BSO crystal is considered as well. Besides the inner capacitances $C^{\bullet}_i$, the ring shaped capacitances $C^{\circ}_i = \varepsilon_i\varepsilon_0\pi(R_2^2 - R_1^2)/d_i$ are calculated. Having the capacitances $C^{\bullet}_i$ for the central area and the capacitances C°_i for the ring, it is important how to combine them. The approach in figure 3(b) considers that the charged particles in the volume are able to move in the lateral direction and that they balance the deviations of the electrical field between the central area and the ring. This means that the lateral component of the electrical field decreases because of the lateral movement of the charged particles. Thus, the discharge connects the central part and the annular part on the upper and lower boundary of the discharge gap. However, the equivalent circuit gives $C^{\bullet+\circ}_{\mathrm{gap}} = C^{\bullet}_{\mathrm{gap}} + C^{\circ}_{\mathrm{gap}}$ for the total gap capacitance. For the upper part and the bottom part, the capacitances of the dielectrics $C^{\mathrm{top}}_{\mathrm{diel}} = C^{\bullet}_{\mathrm{glass1}} + C^{\circ}_{\mathrm{glass1}}$ and

$$C^{\mathrm{bottom}}_{\mathrm{diel}} = \left(\frac{1}{C^{\bullet}_{\mathrm{glass2}}} + \frac{1}{C^{\bullet}_{\mathrm{BSO}}}\right)^{-1} + \left(\frac{1}{C^{\circ}_{\mathrm{glass2}}} + \frac{1}{C^{\circ}_{\mathrm{BSO}}} + \frac{1}{C^{\circ}_{\mathrm{PEEK}}}\right)^{-1} \tag{1}$$

are the sum of two parallel capacitances. The total capacitance of the dielectrics

$$C^{\bullet+\circ}_{\mathrm{diel}} = \frac{C^{\mathrm{top}}_{\mathrm{diel}} C^{\mathrm{bottom}}_{\mathrm{diel}}}{C^{\mathrm{top}}_{\mathrm{diel}} + C^{\mathrm{bottom}}_{\mathrm{diel}}} \tag{2}$$

is the series connection with $C^{\mathrm{top}}_{\mathrm{diel}}$ and $C^{\mathrm{bottom}}_{\mathrm{diel}}$.

In contrast to $C^{\bullet}_{\mathrm{diel}}$ and $C^{\bullet+\circ}_{\mathrm{diel}}$, the total capacitance C_{tot} of the discharge configuration is independent from the chosen equivalent circuit and was derived from the Lissajous figure $Q_{\mathrm{ext}}(U_{\mathrm{ext}})$ during the discharge off-time. It is taken into account the parallel capacitances $C^{\bullet}_{\parallel}$ and $C^{\bullet+\circ}_{\parallel}$ by $C_{\parallel} = C_{\mathrm{tot}} - (C_{\mathrm{diel}}C_{\mathrm{gap}})/(C_{\mathrm{diel}} + C_{\mathrm{gap}})$, which consider the parallel capacitance of the surroundings beyond R_1 and R_2, respectively [33, 34].

Despite C_{gap}, C_{diel}, and $C_{\parallel}$ are different for the two equivalent circuits, the formulas for the calculation of the gap voltage

$$U_{\mathrm{gap}}(t) = U_{\mathrm{ext}}(t)\left(1 + \frac{C_{\parallel}}{C_{\mathrm{diel}}}\right) - \frac{Q_{\mathrm{ext}}(t)}{C_{\mathrm{diel}}}, \tag{3}$$

and the discharge current

$$I_{\mathrm{dis}}(t) = \left(1 + \frac{C_{\mathrm{gap}}}{C_{\mathrm{diel}}}\right)\left(I_{\mathrm{tot}}(t) - C_{\mathrm{tot}}\frac{\mathrm{d}U_{\mathrm{ext}}(t)}{\mathrm{d}t}\right) \tag{4}$$

remain the same as for symmetric discharge configurations [35]. Since both quantities are different for the two equivalent circuits, they are written as $U^{\bullet}_{\mathrm{gap}}$, $I^{\bullet}_{\mathrm{dis}}$ and $U^{\bullet+\circ}_{\mathrm{gap}}$, $I^{\bullet+\circ}_{\mathrm{dis}}$.

2.3. Surface charge diagnostics

The surface charge measurement is based on the electro-optic Pockels effect of the BSO crystal. Figure 2(b) shows the simplified optical setup. In general, elliptically polarized LED light ($\lambda = 634$ nm) passes the discharge cell twice due to reflection at the grounded aluminum mirror. The reflected light intensity is detected by a CCD camera (Phantom Miro 4ex). During the discharge operation, both the applied voltage ($U^{\mathrm{ext}}_{\mathrm{BSO}}$) and the deposited surface charges ($U^{\sigma}_{\mathrm{BSO}}$) induce a birefringence of the BSO crystal. Hence, the elliptical polarization of the transmitted light differs from the incident light. As a result, the detected light intensity depends on the amount and polarity of the surface charges. Finally, the surface charge density

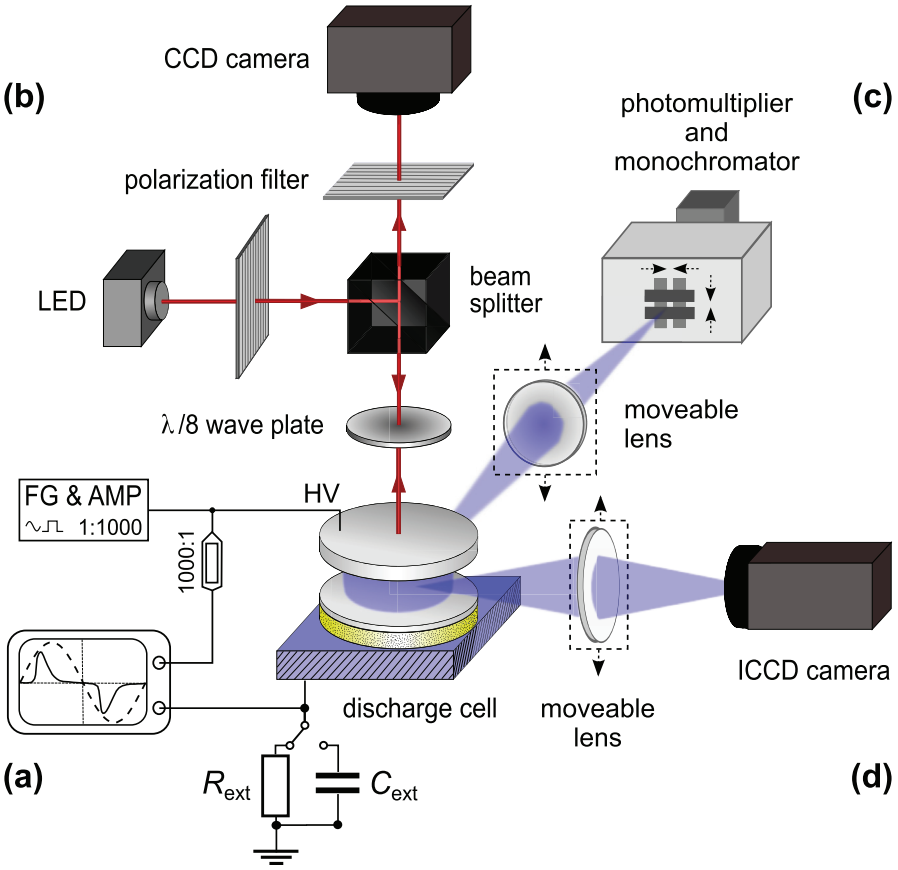

Figure 2. Sketch of the diagnostic setup: (a) electrical measurements, (b) surface charge diagnostics, (c) optical emission spectroscopy and (d) ICCD camera imaging.

$$\sigma_{sur}(x,y,t) = \frac{\varepsilon_0 \varepsilon_{BSO}}{d_{BSO}} \left(\frac{I_{meas}(x,y,t)}{I_{ref}(x,y,t)} - 1 \right) \left(U_{BSO}^{ext}(t) + \frac{1}{2k} \right), \tag{5}$$

was calculated from the ratio between the measured intensity $I_{meas}(x,y,t)$ during the discharge and the reference intensity $I_{ref}(x,y,t)$ without any discharge obtained from a calibration measurement. Here, ε_0, ε_{BSO}, and d_{BSO} denote the electric field constant, and the relative permittivity and thickness of the BSO crystal, respectively. Moreover, k is the slope of the linear dependence of I_{ref} on U_{BSO}^{ext}. Further details are given in [32]. Furthermore, the spatio-temporal development of the gap voltage

$$U_{gap}(x,y,t) = \frac{C_{diel}}{C_{diel} + C_{gap}} U_{ext}(t) - \frac{A}{C_{diel}} \sigma_{sur}(x,y,t) \tag{6}$$

was recalculated from the surface charge density distribution $\sigma_{sur}(x,y,t)$ with respect to the phase of the feeding voltage $U_{ext}(t)$ [34]. Here, A is the area on the dielectric which is imaged by pixel of the camera, where the surface charges are deposited.

2.4. Optical diagnostics

The optical emission from the discharge volume was imaged by a vertically movable lens onto the entrance slit of a monochromator (Acton Research Corporation, SpectraPro-750i). An additional horizontal slit (0.1 mm width) in front of the monochromator enables the spatial resolution. A further lens is movable in steps of 0.05 mm which allows the axial scan of the discharge volume. The wavelength-selected light was then detected by a photomultiplier tube (Hamamatsu R928), and the converted signal was recorded by the digital oscilloscope with a temporal resolution of 0.1 μs.

In addition, the two-dimensional discharge development in the volume was imaged using a gated intensified charge-coupled device (ICCD) camera (Princeton Instruments PI-MAX) with an effective spatial resolution of 0.04 mm and a maximum temporal resolution of 1 ns. In particular, the camera enables the observation of the discharge in lateral direction to investigate radial discharge inhomogeneities.

3. Overview of the multiple current pulse regime

This section is focused on the electrical characterization of the multiple current pulse regime in helium with small admixtures of nitrogen. Exemplary, the sine-wave feeding voltage $U_{ext}(t)$, the gap voltage $U_{gap}(t)$, and the discharge current $I_{dis}(t)$ are plotted in figure 4 for one period of the discharge operated in helium with 2000 ppm nitrogen admixture at the voltage amplitude $\hat{U}_{ext} = 1.3$ kV. For simplification, the calculation of the gap voltage in this section bases on the equivalent circuit in figure 3(a). For these conditions, five current pulses per half-period were observed. The first current pulse is clearly

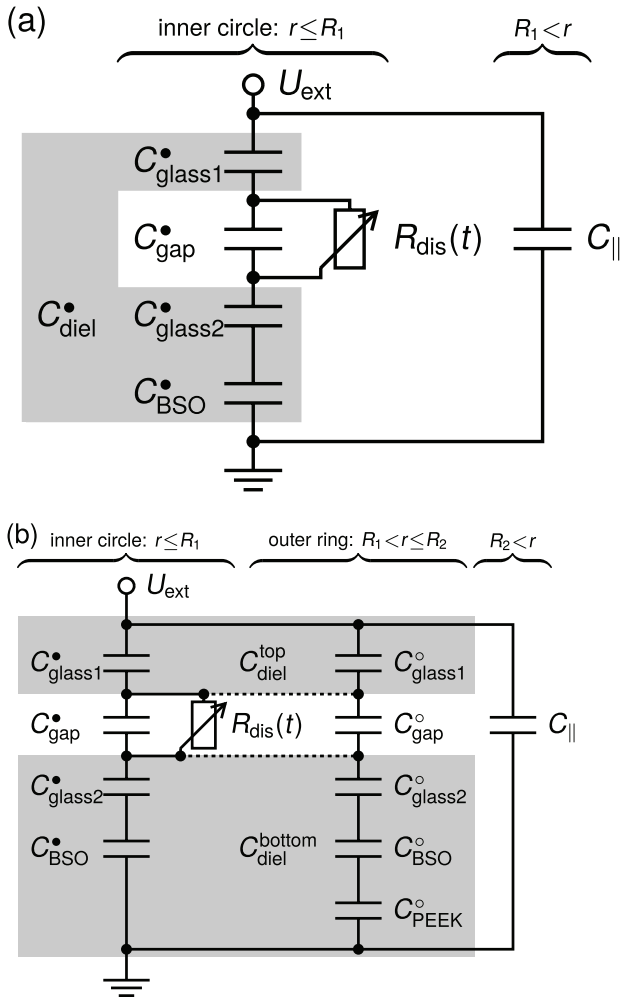

Figure 3. (a) Equivalent circuit diagram considering only the circular central electrode area and (b) equivalent circuit diagram considering the circular central electrode area and the surrounding ring. Further details are given in the text.

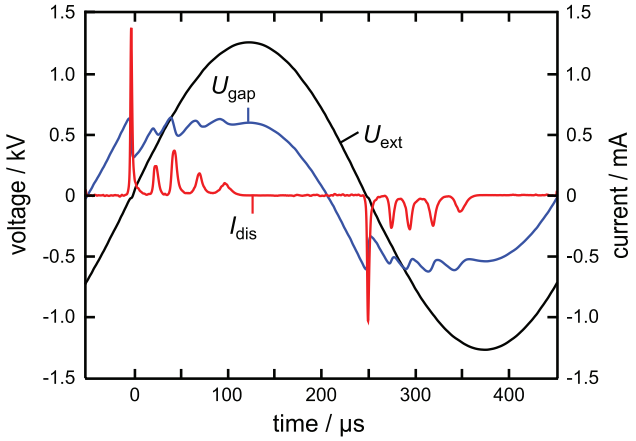

Figure 4. Applied voltage $U_{ext}(t)$, gap voltage $U_{gap}(t)$ and discharge current $I_{dis}(t)$ for the multiple current pulse regime in He + 2000 ppm N_2, $\hat{U}_{ext} = 1.3$ kV.

the largest but has the shortest duration which is correlated with the maximum slope of the feeding voltage in its zero-crossing point. Note that the gap voltage at this time already

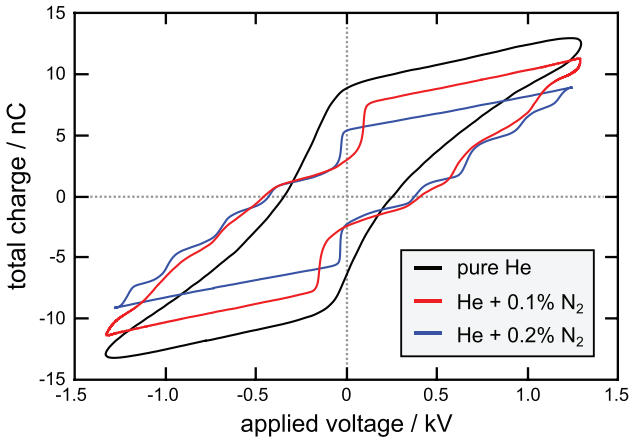

Figure 5. Charge-voltage plots for the discharge in nominally pure He, in He with 1000 ppm N_2 admixture and in He with 2000 ppm N_2 admixture at otherwise constant feeding voltage amplitude of $\hat{U}_{ext} = 1.3$ kV.

exceeds 0.6 kV due to the additional electric field caused by surface charges deposited from previous breakdowns, which is referred to as the surface memory effect. In comparison to the first breakdown, the following current pulses are characterized by much smaller peak values and longer durations, wherein the last pulse occurs just before the applied voltage maximum is reached. After the large but fast drop in gap voltage during the first most intensive discharge breakdown, the applied voltage rises continuously wherefore the gap voltage that is required for discharge breakdown is reached again. The amount of transported and subsequently deposited charge per breakdown is not large enough to prevent further discharge breakdowns within the same half-period. The resulting drop in gap voltage can be obviously compensated for several times as long as the applied voltage increases, resulting in the multiple current pulse regime. However, the weak breakdowns are correlated with the decreasing voltage slope.

In figure 5, the charge-voltage plots (Lissajous figures) are shown for different nitrogen concentrations in helium background gas at an otherwise constant feeding voltage amplitude. The overall amount of transported charge decreases with an increasing nitrogen admixture to helium. The reason is, that the duration of the current pulses is significantly shorter in spite of the enhanced effective ionization rate in the presence of nitrogen admixtures to helium. But, a further increase in the nitrogen content within the percentage range demands higher feeding voltage amplitudes for the discharge operation. This increase in voltage amplitude results in a monotonous increase in the amount of transported charge [29].

The variation of the feeding voltage amplitude or the nitrogen admixture to helium changes the number of current pulses per half-period, as depicted in the existence diagram in figure 6. The following observations were made under the presented discharge conditions: The increase in feeding voltage amplitude results in (i) a steeper voltage slope and thus in a shorter current pulse duration, (ii) an earlier compensation of the gap voltage drop after each discharge event, and (iii) a shift of the gas-specific breakdown voltage to an earlier phase of the sine-wave operation. In sum, the breakdown condition

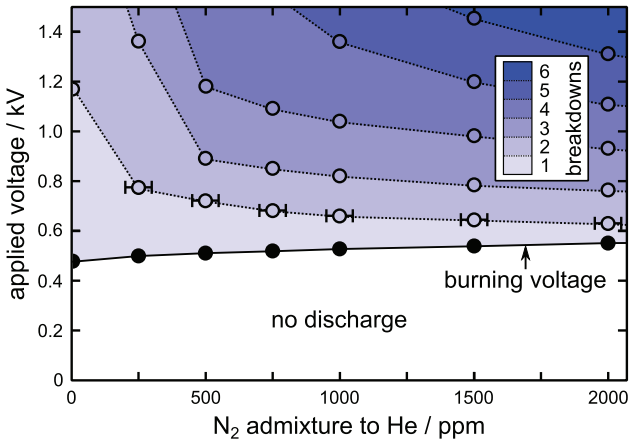

Figure 6. Existence diagram for the multiple current pulse regime: number of stationary breakdowns depending on the N_2 admixture to He and the applied voltage amplitude.

is reached more often which corresponds to an increase in the number of current pulses per half-period.

The effect of the increasing nitrogen admixture on the number of current pulses is more complicated. At these low nitrogen admixtures, the Penning-ionization

$$N_2 + He^m/He_2^m \rightarrow N_2^+ + e^- + He/2He, \qquad (7)$$

plays a key role in the ionization dynamics. It slows down the ionization dynamics and supports the lateral homogenization of the diffuse discharge. On the one hand, the increase in nitrogen admixtures enhances the Penning-ionization rate, but on the other hand, the lifetime of helium metastable atoms $He^m = He(3^3S)$ and molecules $He_2^m = He_2(a^3\Sigma_u^+)$ decreases. In addition, the electron impact excitation of He^m becomes less effective due to the loss of high-energy electrons by excitation of vibrational electronic levels of nitrogen molecules. Besides, the direct electron impact ionization of nitrogen molecules becomes more important for larger nitrogen admixtures. In general, due to the importance of electron-impact processes during the breakdown, the discharge current is determined by the gap voltage drop and vice versa. Probably, for the multiple current pulse regime observed here, the slow Penning-ionization still dominates, but the decreased metastables lifetime results in a shortening of the discharge current pulses. Hence, less charges are transported during one current pulse and the drop in gap voltage is lower for larger nitrogen admixtures. Therefore, the ignition gap voltage is reached earlier after a discharge current pulse and the number of current pulses per half-period increases.

Even in nominally pure helium (purity $> 99.999\%$), the air impurity concentration is in the order of 100 ppm which enables a maximum of two discharge breakdowns per half-period without external admixture of nitrogen. Finally, a further increase in feeding voltage amplitude or nitrogen concentration causes the transition to the microdischarge regime favored by (i) a steep voltage slope which allows the discharge ignition at over-voltage, and by (ii) a larger effective ionization coefficient. Thus, the multiple stationary breakdowns represent the intermediate regime between the classical diffuse barrier discharge with one current pulse per half-period and the non-homogeneous and non-stationary filamentary barrier discharge. This was also observed for barrier discharges in helium-oxygen mixtures [30], where Penning ionization of oxygen dominates the discharge too, as well as in nitrogen-oxygen mixtures [23, 36], where nitrogen metastable states are effectively quenched by oxygen.

4. Breakdown mechanism

This section reports on the breakdown mechanisms of the consecutive single discharge events in the multiple current pulse regime. Figure 7 shows the spatio-temporal discharge development for a full sine-wave voltage period, comparing the operation in pure helium (purity $> 99.999\%$) on the left side (figures 7(a)–(c)) with the operation in helium with 2000 ppm nitrogen admixture on the right side (figures 7(d)–(f)). In both cases, the feeding voltage amplitude amounts to $\hat{U}_{ext} = 1.3$ kV. In (a) and (d), the sine-wave feeding voltage $U_{ext}(t)$, the gap voltage $U_{gap}(t)$ and discharge current $I_{dis}(t)$ are plotted. Starting with the discussion of the discharge operated in nominally pure helium, two breakdowns per half-period can be identified. The first breakdown is characterized by much larger current pulse and drop in gap voltage than the second breakdown. The latter is very weak and starts just before the feeding voltage amplitude is reached. In (b), the spatio-temporal development of the optical emission is depicted for the band head of the first negative system (FNS) $N_2^+(B^2\Sigma_u^+ \rightarrow X^2\Sigma_g^+)$ at 391.4 nm and for the transition $He(3^3S \rightarrow 2^3P)$ at 706.5 nm. Here, the emission of the N_2^+ ion is taken because it is dominantly populated via Penning ionization (equation (7)) by helium metastable states. Hence, it traces the helium metastables density. For comparison, the He I line acts as an indicator for both high electric field and high electron density, and thus for a high ionization rate, because the electron-impact excitation of the helium ground state

$$He + e^- \rightarrow He(3^3S) + e^- \qquad (8)$$

with the high excitation energy of 22.4 eV is the dominant production channel. Finally, figure 7(c) zooms into the He I emission of (b) for the first discharge breakdown.

Looking at the optical emission, both the N_2^+ FNS band head and the He I line show a global emission maximum in front of the cathodic dielectric for the first breakdown and a local He I emission maximum near to the anodic dielectric during the second breakdown. Furthermore, the first breakdown reveals a cathode-directed development of the He I emission starting during the pre-phase in front of the anode. The results indicate that the first intensive discharge breakdown is glow-like. The glow-like discharge is characterized by significant distortion of the electric field across the gas gap due to positive space charge formation, resulting in the cathode fall region and the negative glow at the time of the current maximum [18, 37–39]. However, the second weak discharge breakdown is Townsend-like. Typically, the Townsend-like discharge is operated in pure nitrogen, or in helium for small discharge gap widths [11, 19, 20, 40]. In Townsend-like discharges, the gradual charge carrier production is efficient enough for a breakdown

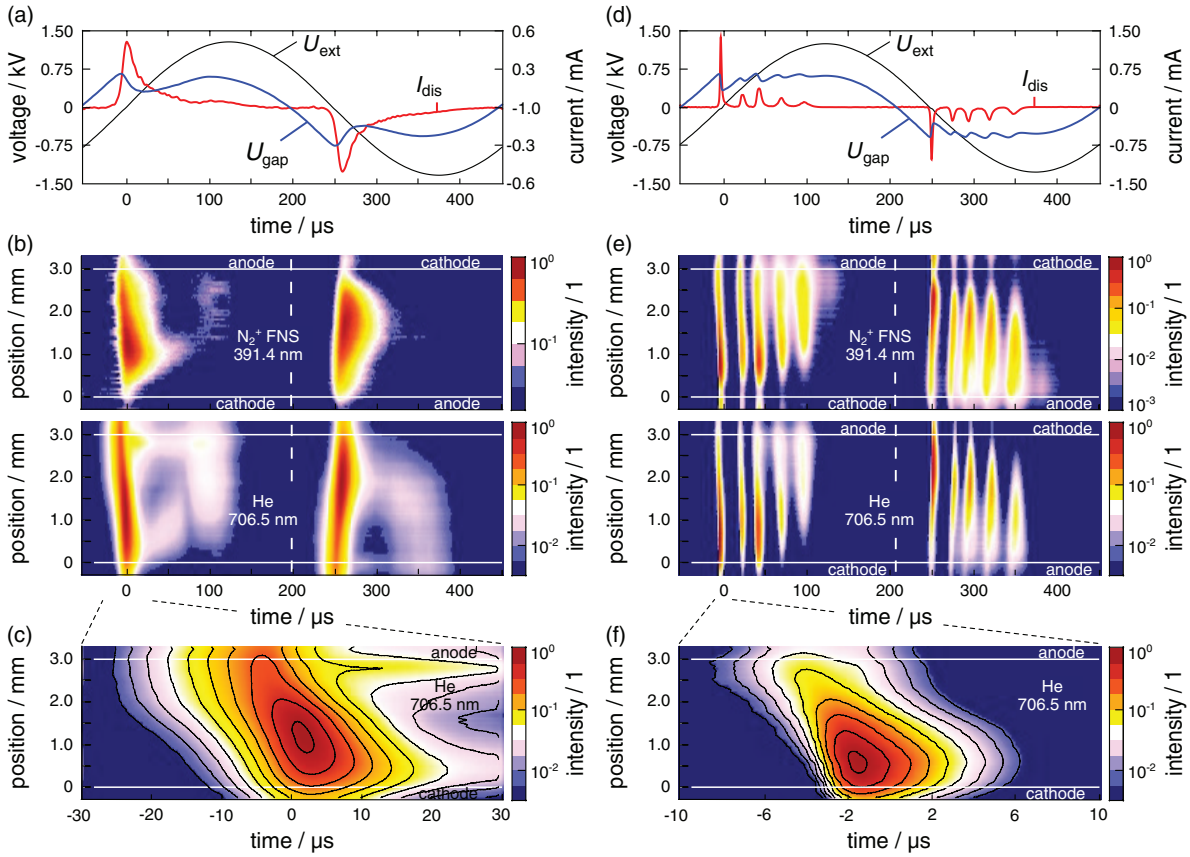

Figure 7. Spatio-temporal discharge development in nominally pure He (left) and in He with 2000 ppm N_2 admixture (right) at the feeding voltage amplitude $\hat{U}_{ext} = 1.3$ kV: (a) sine-wave feeding voltage $U_{ext}(t)$ and discharge current $I_{dis}(t)$ for one discharge period, (b) spatio-temporally resolved emission of N_2^+ first negative system (FNS) at 391.4 nm and He I at 706.5 nm, and (c) zoom into the spatio-temporal emission of He I for the first discharge breakdown.

at low electric fields without significant space charge formation, hence the electric field across the gas gap keeps nearly constant. Here, especially the flat feeding voltage slope and the enhanced secondary electron emission by residual ions and the Penning-ionization by metastable states from the first breakdown favor the formation of the second Townsend-like breakdown. The presence of residual species in the volume during the pre-phase of the second breakdown is indicated by the long-lasting optical emission in figure 7(b).

Taking a closer look on the discharge in helium with 2000 ppm nitrogen admixture in figure 7(d), five current pulses were detected, wherein the first one is again much more intensive than the following ones. The current pulse duration is much shorter than for the discharge in nominally pure helium. This is caused by the decrease in the effective lifetime of helium metastable states participating in Penning ionization (7) of nitrogen admixtures, as already discussed in the previous section. With consideration of the rate coefficient $k_{PI} = 7 \times 10^{-11}$ cm^3 s^{-1} for Penning ionization of N_2 [41–44], and the total pressure of 500 mbar, the effective lifetime of He^m decreases from about 10 μs in helium (assumption of about 100 ppm nitrogen impurities) to less than 1 μs in helium with 2000 ppm nitrogen admixture. Moreover, compared to the discharge in helium, the optical emission in (e) and (f) reveals a faster propagation of the ionization front as well as a smaller extent of the cathode fall region for the first intensive breakdown. Regarding the following breakdowns, the ionization front is slower and has its maximum farther away from the cathodic dielectric. For the last two breakdowns, the maximum in optical emission is clearly shifted towards the anode. Hence, there is a transition from the first breakdown operating in the glow mode to the last breakdown operating in the Townsend mode.

5. Lateral distribution of multiple breakdowns

This section reports on the two-dimensional discharge development in the volume, the spatio-temporal development of the gap voltage, and the lateral surface charge distribution for the multiple current pulse regime of the diffuse discharge in He with a N_2 admixture of 2000 ppm.

A first indication of the lateral discharge development yields from the results of the spatially resolved and temporally averaged optical emission, as shown for the first three discharge pulses during the positive half period in figure 8. All three images have their maximal intensity in front of the cathode, which reflects the increase in electric field strength during the cathode-directed ionizing front. The increase in intensity towards the cathode is steeper for the discharge pulses P1 and P3, and flatter for P2. The position of the cathode ($z = 0$ mm) in figure 8 is defined using the reflexion edge of the emission

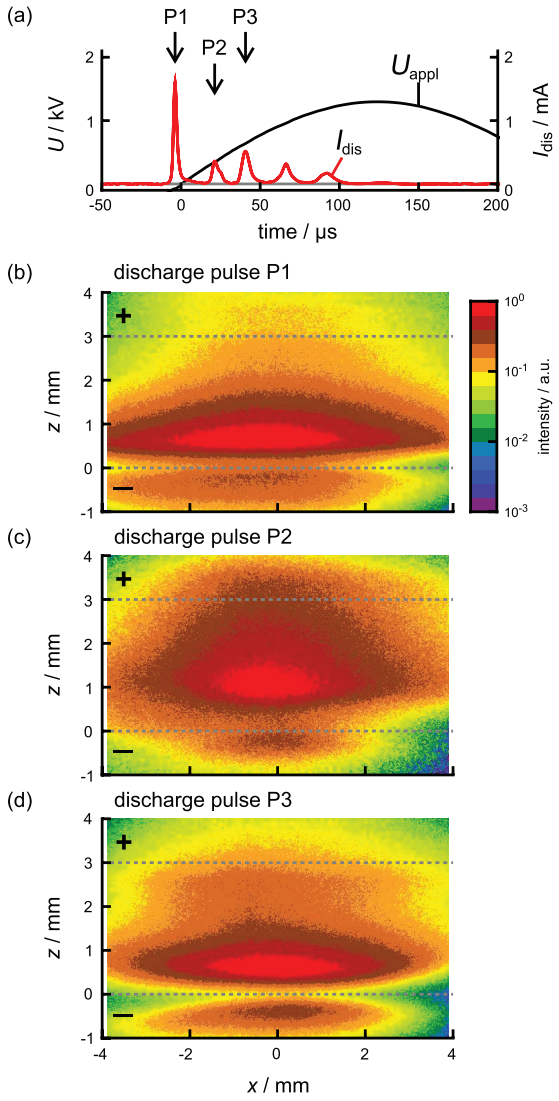

Figure 8. (a) Applied voltage and discharge current of multiple diffuse breakdowns in helium with 2000 ppm N_2 at 500 mbar. ((b)–(d)) Corresponding temporally averaged optical emission of the first three discharge pulses.

from the discharge pulses P1 and P3. The reflexion edge of discharge pulse P2 is less pronounced and shifted, which indicates that the maximal intensity comes from an area outside the focus of the ICCD camera measurement.

Looking at the lateral distribution of the intensities, all current pulses have their maximum intensity at $x = 0$ mm. Because of the line of sight measurement, this does not imply that the maximal intensity of the discharge current pulse is actually on the symmetry axis of the discharge configuration. For a clearer statement, an Abel inversion would be necessary, but the gap spacers in the discharge configuration limit the lateral extension of the observation window.

Overall, the ICCD camera measurements cannot support the results from Mangolini *et al* that consecutive breakdowns per half-period appear in different radial symmetrical regions [26]. Therefore, the method of surface charge measurement is taken to confirm the results from Mangolini *et al*, which is discussed in the following. The laterally resolved surface charge measurement presented in figure 9(a) allows the calculation of the two-dimensional gap voltage distribution at a given time by equation (6), as shown in figure 9(b). Roughly two regions of different gap voltage values are visible. The inner circle which is given by the diameter of the aluminum mirror (compare figure 1) shows an average gap voltage of about 250 V with a slight increase towards the left bottom corner. The calculated gap voltage of the surrounding ring is much higher and up to 1400 V at the edge between the inner circle and the ring. Such a large voltage is not conceivable, a discharge would immediately ignite at this position. Hence, the calculation of the gap voltage is inappropriate for the outer ring.

The calculation of the static electric field strength distribution for the discharge cell configuration via COMSOL multiphysics® software, as presented in figure 10, explains this discrepancy. It shows a radial-symmetric sketch of the discharge cell configuration. The amount of the electric field strength is indicated by the background color and the direction by the solid lines, respectively. For the inner part of the gas gap and the dielectrics ($r \leqslant 7.5$ mm), the electric field is homogeneous. Beyond the radius of the bottom electrode, this homogeneity is slightly distorted, but no field enhancement as calculated in figure 9(b) is visible. The reason is the wrong assumption of the model in equation (6), that the axial electric field in the BSO crystal is parallel to the symmetry axis of the discharge configuration. In contrast, the electric field lines in the BSO crystal are directed towards the grounded electrode in the center. Due to the complex electric field distribution for the outer ring, it is not recommended to calculate the gap voltage near the edges by equation (6). Therefore, the gap voltage in the outer ring is not considered in the further discussion. In contrast, the effect of distorted field lines on the surface charge density measurements is low due to much lower voltage drop U_{BSO}^{ext} over the dielectric BSO. Furthermore, calibration measurements minimize the influence of the applied voltage on the surface charge measurement [32]. Having both the spatially resolved surface charge density σ and the gap voltage U_{gap}, it is possible to compare these quantities for the subsequent discharge current pulses. Such laterally resolved measurements are shown in figure 11(a) for the discharge current pulses P1 to P5 during the positive half-period and in figure 11(b) for the discharge current pulses N1 to N5 of the negative half-period, respectively. Both figures each with three columns represent the absolute gap voltage $|U_{gap}|$ and the surface charge density σ before the current pulse, as well as the change of surface charge density $\Delta\sigma$ during the discharge current pulse. The spatially averaged values are shown in the respective top left corner, and the rows represent the five subsequent discharge current pulses.

In principal, the results for P1, P3, P4, N1, N2, and N3 show a similar behavior. The surface charges deposited from a previous breakdown act as fingerprint for the gap voltage and re-ignition of the following breakdown [29, 32, 45]. This is clearly visible in the change of the surface charge density $\Delta\sigma$, calculated from the difference after and before the current pulse. The most charges were transferred and deposited in regions where the gap voltage is highest.

P2, P5, N4, and N5 deviate from the description above. In fact, the gap voltage shows the same distribution as the

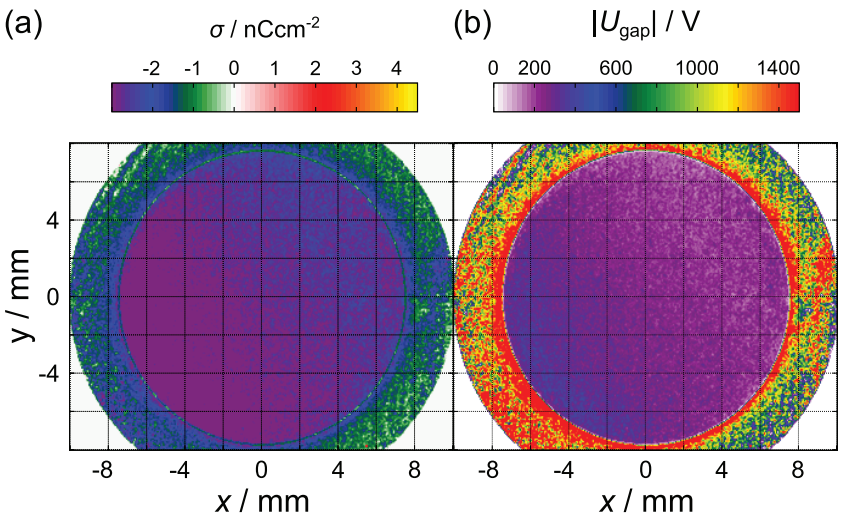

Figure 9. Lateral distribution of (a) surface charge density and (b) spatially resolved gap voltage across the bottom dielectric area including the centered bottom electrode area. Both were recorded at $t = -10.6$ μs; compare figure 4.

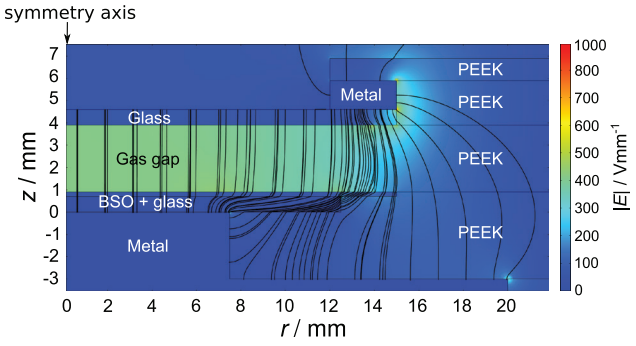

Figure 10. Static electric field distribution for the discharge cell configuration calculated with COMSOL multiphysics. The applied voltage is 1.3 kV.

surface charge density before a current pulse, but these discharge breakdowns do actually not occur in regions where the absolute value of the gap voltage has its maximum. In particular, this is clearly seen in case of P2. Here, the difference of surface charge $\Delta\sigma$ shows an annular structure. The reason might be the electric field enhancement at the electrode edge. A second hint could be the weak current at the end of the first breakdown which is very close to the second breakdown. The needed seed electrons for re-ignition of the second breakdown are probably provided by secondary electron emission by ions hitting on the cathode. An interpretation in the same manner is possible for the results in the change of the surface charge density in case of P5, N4, and N5.

Regarding the positive half-period, the discharge operates alternately at different concentric regions of the electrode, except for the second breakdown. These results are in agreement with measurements performed by Mangolini *et al* where the discharge operates during two consecutive current pulses on different lateral regions of the electrode configuration [26]. In the negative half-period, the single breakdowns occur also at different regions of the electrode, but not alternately as in the positive half-period. The different diameters of the electrodes and dielectrics are probably responsible for the different behavior in the positive and negative half cycle.

6. Comparison of spatially resolved measurements with global electrical description

In this section the results of the global gap voltage calculation, based on electrical equivalent circuit diagrams, are discussed with gap voltage determination from the spatially resolved surface charge measurements.

The global gap voltage is shown in figure 12 for different electrical equivalent circuits, as discussed in section 2.2. The gap voltage $U^{\bullet}_{\mathrm{gap}}$ bases on the equivalent circuit shown in figure 3(a). Here, it was assumed that the discharge is limited on the bottom electrode radius $R_1 = 7.5$ mm. The gap voltage $U^{\bullet+\circ}_{\mathrm{gap}}$ is calculated for the extended equivalent circuit, as shown in figure 3(b). It considers a larger discharge area limited by the BSO crystal with a radius of $R_2 = 12.5$ mm. $U^{\bullet}_{\mathrm{gap}}$ and $U^{\bullet+\circ}_{\mathrm{gap}}$ decrease fast and strongly during the first current pulse but with a large difference in ignition voltage. $U^{\bullet}_{\mathrm{gap}}$ reaches after the breakdown the same value as before, which is necessary for the discharge re-ignition. In case of $U^{\bullet+\circ}_{\mathrm{gap}}$ the voltage value for re-ignition is higher than before. The gray colored area represents the gap voltage range between $U^{\bullet}_{\mathrm{gap}}$ and $U^{\bullet+\circ}_{\mathrm{gap}}$. The laterally averaged gap voltage $U^{\sigma}_{\mathrm{gap}}$ is calculated with equation (6) from the measured surface charge density and corresponds to the gap voltage shown in figure 11. $U^{\sigma}_{\mathrm{gap}}$ lies in between the curves from the equivalent circuits. Mostly, it is closer to the curve $U^{\bullet+\circ}_{\mathrm{gap}}$. Hence, the equivalent circuit in figure 3(b) is more appropriate to estimate the gap voltage from the global external quantities, because it shows that the ignition voltage increases for the subsequent current pulses. One explanation might be the removal of weakly bound surface electrons deposited during the previous breakdowns. As a consequence, the pre-ionization before and secondary electron emission during the breakdown should be reduced.

The development of the spatially averaged charge Q deposited on the BSO crystal is shown in figure 13. The transported charge Q_{dis} during a breakdown results from the temporally integrated net current I_{dis}, which is also shown in figure 13. The different curves representing Q base on the

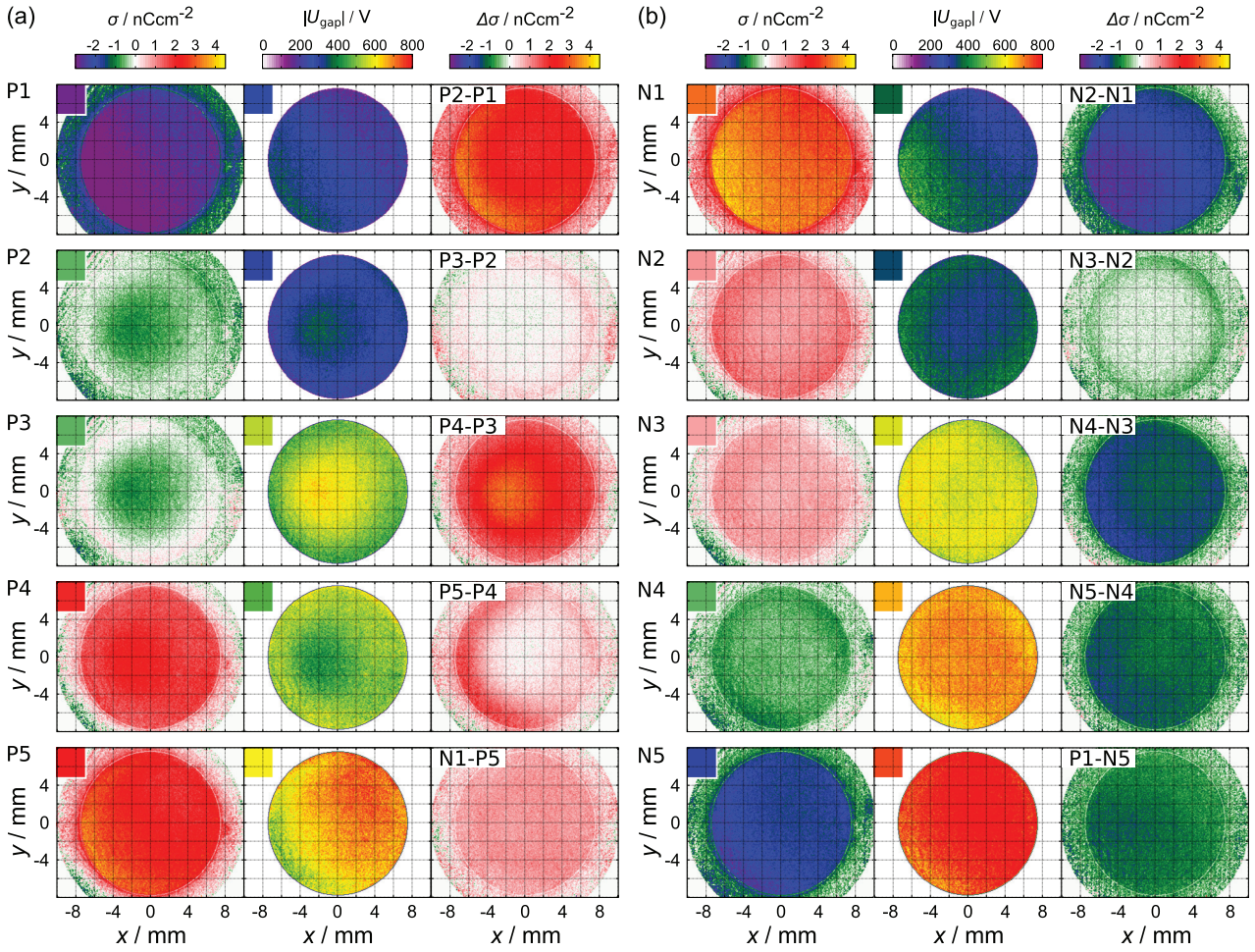

Figure 11. (a) Measurement times P1, ..., P5 in positive half-period. (b) Measurement times N1, ..., N5 in negative half-period. Left column: surface charge density σ, middle column: absolute gap voltage $|U_{\mathrm{gap}}|$, right column: change of surface charge density $\Delta\sigma$ due to a current pulse.

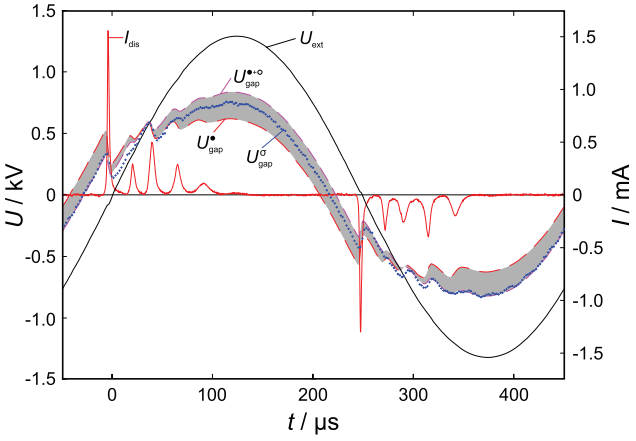

Figure 12. Comparison of different gap voltage calculations. The gap voltage $U^{\bullet}_{\mathrm{gap}}$ bases on the equivalent circuit shown in figure 3(a). The voltage $U^{\bullet+\circ}_{\mathrm{gap}}$ is calculated for the extended equivalent circuit shown in figure 3(b). The gap voltage $U^{\sigma}_{\mathrm{gap}}$ bases on the surface charge measurement performed on the entire electrode. The gray area marks possible gap voltages between these two models. The discharge is operated in helium with an admixture of 2000 ppm nitrogen at 500 mbar. The applied voltage amplitude is 1.3 kV.

same surface charge measurement, which is performed on the entire dielectric. However, $Q^{\bullet}_{\mathrm{square}}$ and $Q^{\bullet}$ are averaged on an estimated discharge area, which was used in [32]. $Q^{\bullet}_{\mathrm{square}}$ is averaged on a centered square with 8.2 mm × 8.2 mm side length. The amount of the surface charge on that area was extrapolated on the area of the grounded electrode ($\varnothing = 15$ mm, $A = 1.77$ cm^2) to calculate the total amount of charge deposited on the dielectric surface. For this purpose, the assumption of a homogeneous surface charge distribution was made. Instead, $Q^{\bullet}$ mirrors the surface charge measurement on the entire grounded electrode area without any extrapolation. Both $Q^{\bullet}$ and $Q^{\bullet}_{\mathrm{square}}$ show a good qualitative agreement for the complete period, but the absolute values are much lower than the transferred charge Q_{dis}. In particular, the second current pulse is scarcely depicted. The comparison of the transported charge Q_{dis} with the surface charge $Q^{\bullet+\circ}$ deposited on the entire dielectric is in good qualitative agreement. This supports the assumption that the remaining surface charge is deposited on the outer dielectric ring of the discharge cell configuration. But for $Q^{\bullet+\circ}$, a discrepancy exists for the two first discharge current pulses in both polarities. The amount of deposited surface charge $Q^{\bullet+\circ}$

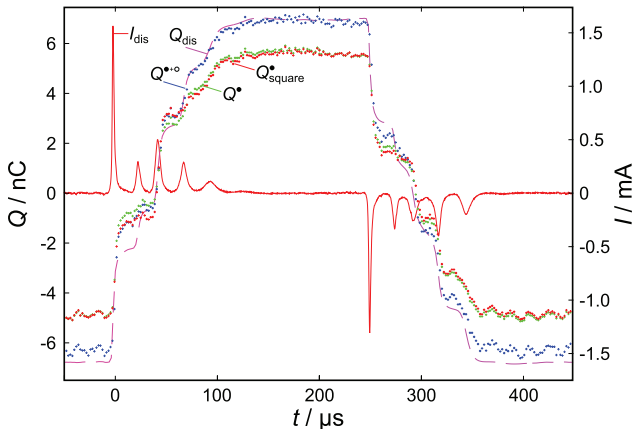

Figure 13. Temporally integrated net current I_{dis} and phase resolved surface charge for different discharge areas. $Q^{\bullet}_{square}$ is averaged on a square with 8.2 mm × 8.2 mm side length and extrapolated on the area of the grounded electrode. $Q^{\bullet}$ covers the grounded electrode with a diameter of 15 mm. $Q^{\bullet+\circ}$ is measured on the entire dielectric. The applied voltage is 1.3 kV. The discharge is operated in helium with an admixture of 2000 ppm nitrogen at 500 mbar. The applied voltage is 1.3 kV.

increases significantly when the first current pulse becomes rather weak at the end, and it is too low for the second current pulse. This deviation might be due to the electric field enhancement at the edge of the grounded electrode edge, as shown in figure 10. Despite careful measurements and estimations, the electric field enhancement in the region of the edge could adversely affect the surface charge measurement. But all in all, the outer dielectric ring must be considered for surface charge deposition which improves the surface charge measurement qualitatively and quantitatively.

7. Conclusions

The presented paper is a consistent extension of the authors previous works. The experimental setup, especially the discharge cell configuration, was improved allowing the joint investigation of volume and surface processes of a barrier discharge (BD) operated in the multiple current pulse regime under well-defined and identical conditions. In particular, the optical emission spectroscopy and ICCD imaging allow the measurement of the spatio-temporal and spectrally resolved discharge development in the volume, whereby conclusions can be drawn about the breakdown mechanism of the discharge. The laterally and temporally resolved development of surface charges on the BSO crystal is investigated with the help of the electro-optic Pockels effect. The investigations are completed by electrical measurements.

The diffuse discharge was systematically investigated in helium with nitrogen admixtures for a plane-to-plane configuration with a gap distance of 3 mm. Depending on the nitrogen content and the applied voltage amplitude, the number of current pulses per half-period varies. For a low voltage amplitude only one discharge current pulse appears which operates in the glow-like discharge mode. An increase of the applied voltage results in a multiple current pulse regime. For this regime, the first current pulse is glow-like, hence, the intensity maximum is located in front of the cathode. The maximum emission intensity in the gap is shifted with a higher number of current pulses towards the anode and becomes weaker. The last current pulse is Townsend-like. Comparing a discharge in helium-nitrogen mixtures with a discharge operated in pure helium, the current pulse duration is shorter and the gap voltage drop is reduced. One reason is a decrease of the effective lifetime of helium metastable states participating in Penning ionization. The higher the nitrogen admixture to helium the faster is the propagation of the ionization front and the shorter is the cathode fall region for the first breakdown. Further breakdowns last longer and their optical emission is shifted towards the anode indicating the transition to a Townsend-like discharge.

The surface charge measurement on glass as dielectric was successfully established with a high sensitivity. Furthermore, the improved design of the discharge cell configuration enabled the surface charge measurement on the entire dielectric. It turned out that the discharge ignites on different areas depending on the previous surface charge distribution and spatial gap voltage distribution. Two lateral structures are preferred: The discharge ignites either in the center of the electrode arrangement or ring-shaped close to the edges of the metallic electrode. Besides, the phase resolved surface charge development is correlated with the net current. For the multiple current pulse regime, the laterally integrated phase resolved development of the surface charge shows a good agreement with the temporally integrated net current when the entire dielectric area is considered. This shows the importance to pay attention on the complete area of the electrode arrangement. Furthermore, the different spatial distribution of the discharge current pulses inhibits a calculation of the spatio-temporally resolved gap voltage based on an appropriate electrical equivalent circuit. In particular, the edges of the electrodes provide lateral field components which cannot be considered by simple equivalent circuits. The comparison of the spatially resolved gap voltage and surface charge shows that the field enhancement by residual surface charges is the main reason for the lateral distribution of the first discharge current pulse (surface memory effect). But the subsequent current pulses do not always follow the surface charge distribution. Here, the electric field distortion at the edges of the electrodes or metastables from the previous discharge current pulses become important.

Acknowledgment

The authors thank Hans-Erich Wagner for the important ideas leading to this work and for his fruitful discussions. The work was supported by Deutsche Forschungsgemeinschaft, Collaborative Research Centre 24 (TRR24) ‘Fundamentals of Complex plasmas’, project B11.

References

[1] Samoilovich V G, Gibalov V I and Kozlov K V 1997 *Physical Chemistry of the Barrier Discharge* (Düsseldorf: DVS Media GmbH)

[2] Kogelschatz U 2003 Dielectric-barrier discharges: their history, discharge physics, and industrial applications *Plasma Chem. Plasma Process.* **23** 1–46

[3] Wagner H-E, Brandenburg R, Kozlov K V, Sonnenfeld A, Michel P and Behnke J F 2003 The barrier discharge: basic properties and applications to surface treatment *Vacuum* **71** 417–36 (*Symp. on Plasma Surface Engineering at the Spring Meeting of the German Physical Society (Regensburg, Germany, 11–15 March 2002)*)

[4] Becker K H, Kogelschatz U, Schoenbach K H and Barker R J 2004 *Non-Equilibrium Air Plasmas at Atmospheric Pressure* (*Series in Plasma Physics*) (Bristol: Institute of Physics Publishing)

[5] Laroussi M 2005 Low temperature plasma-based sterilization: overview and state-of-the-art *Plasma Process. Polym.* **2** 391–400

[6] Fridman G, Friedman G, Gutsol A, Shekhter A B, Vasilets V N and Fridman A 2008 Applied plasma medicine *Plasma Process. Polym.* **5** 503–33

[7] Bruggeman P and Leys C 2009 Non-thermal plasmas in and in contact with liquids *J. Phys. D: Appl. Phys.* **42** 053001

[8] Weltmann K D, Kindel E, von Woedtke T, Hähnel M, Stieber M and Brandenburg R 2010 Atmospheric-pressure plasma sources: prospective tools for plasma medicine *Pure Appl. Chem.* **82** 1223–37

[9] Kozlov K V, Wagner H-E, Brandenburg R and Michel P 2001 Spatio-temporally resolved spectroscopic diagnostics of the barrier discharge in air at atmospheric pressure *J. Phys. D: Appl. Phys.* **34** 3164

[10] Wagner H-E, Brandenburg R and Kozlov K V 2004 Progress in the visualization of filamentary gas discharges. Part 1: milestones and diagnostics of dielectric-barrier discharges by cross-correlation spectroscopy *J. Adv. Oxid. Technol.* **7**

[11] Brandenburg R, Maiorov V A, Golubovskii Y B, Wagner H-E, Behnke J and Behnke J F 2005 Diffuse barrier discharges in nitrogen with small admixtures of oxygen: discharge mechanism and transition to the filamentary regime *J. Phys. D: Appl. Phys.* **38** 2187

[12] Hoder T, Scaroníra M, Kozlov K V and Wagner H-E 2009 3d imaging of the single microdischarge development in coplanar barrier discharges in synthetic air at atmospheric pressure *Contrib. Plasma Phys.* **49** 381–7

[13] Höft H, Kettlitz M, Becker M M, Hoder T, Loffhagen D, Brandenburg R and Weltmann K-D 2014 Breakdown characteristics in pulsed-driven dielectric barrier discharges: influence of the pre-breakdown phase due to volume memory effects *J. Phys. D: Appl. Phys.* **47** 465206

[14] Kanazawa S, Kogoma M, Moriwaki T and Okazaki S 1988 Stable glow plasma at atmospheric pressure *J. Phys. D: Appl. Phys.* **21** 838

[15] Okazaki S, Kogoma M, Uehara M and Kimura Y 1993 Appearance of stable glow discharge in air, argon, oxygen and nitrogen at atmospheric pressure using a 50 Hz source *J. Phys. D: Appl. Phys.* **26** 889

[16] Trunec D, Brablec A and Šťastný F 1998 Experimental study of atmospheric pressure glow discharge *Contrib. Plasma Phys.* **38** 435–45

[17] Massines F, Ségur P, Gherardi N, Khamphan C and Ricard A 2003 Physics and chemistry in a glow dielectric barrier discharge at atmospheric pressure: diagnostics and modelling *Surf. Coat. Technol.* **174** 8–14

[18] Navrátil Z, Brandenburg R, Trunec D, Brablec A, St'ahel P, Wagner H-E and Kopecký Z 2006 Comparative study of diffuse barrier discharges in neon and helium *Plasma Sources Sci. Technol.* **15** 8

[19] Golubovskii Y B, Maiorov V A, Li P and Lindmayer M 2006 Effect of the barrier material in a townsend barrier discharge in nitrogen at atmospheric pressure *J. Phys. D: Appl. Phys.* **39** 1574

[20] Gherardi N, Gouda G, Gat E, Ricard A and Massines F 2000 Transition from glow silent discharge to micro-discharges in nitrogen gas *Conf. Proc. 16th Intern. Symp. on Plasma Chem. (Taormina, Italy)* **9** 340

[21] Bibinov N K and Wiesemann K (ed) 2003 *Filamentary and Homogeneous Dielectric Barrier Discharges in He/N_2 Mixtures at Atmospheric Pressure*

[22] Naudé N, Cambronne J-P, Gherardi N and Massines F 2005 Electrical model and analysis of the transition from an atmospheric pressure Townsend discharge to a filamentary discharge *J. Phys. D: Appl. Phys.* **38** 530

[23] Brandenburg R, Navrátil Z, Jánský J, St'ahel P, Trunec D and Wagner H-E 2009 The transition between different modes of barrier discharges at atmospheric pressure *J. Phys. D: Appl. Phys.* **42** 085208

[24] Bogaczyk M, Sretenovi G B and Wagner H-E 2013 Influence of the applied voltage shape on the barrier discharge operation modes in helium *Eur. Phys. J.* D **67** 1–11

[25] Akishev Y S, Dem'yanov A V, Karal'nik V B, Pan'kin M V and Trushkin N I 2001 Pulsed regime of the diffusive mode of a barrier discharge in helium *Plasma Phys. Rep.* **27** 164–71

[26] Mangolini L, Orlov K, Kortshagen U, Heberlein J and Kogelschatz U 2002 Radial structure of a low-frequency atmospheric-pressure glow discharge in helium *Appl. Phys. Lett.* **80** 1722–4

[27] Radu I, Bartnikas R and Wertheimer M R 2005 Diagnostics and modelling of noble gas atmospheric pressure dielectric barrier discharges in homogeneous or diverging electric fields *J. Phys. D: Appl. Phys.* **38** 539

[28] Ha Y, Wang H and Wang X 2012 Modeling of asymmetric pulsed phenomena in dielectric-barrier atmospheric-pressure glow discharges *Phys. Plasmas* **19** 021308

[29] Tschiersch R, Bogaczyk M and Wagner H-E 2014 Systematic investigation of the barrier discharge operation in helium, nitrogen, and mixtures: discharge development, formation and decay of surface charges *J. Phys. D: Appl. Phys.* **47** 365204

[30] Dosoudilov L, Tschiersch R, Bogaczyk M, Navr Z, Wagner H-E and Trunec D 2015 Investigation of helium barrier discharges with small admixtures of oxygen *J. Phys. D: Appl. Phys.* **48** 355204

[31] Bai Z, Wang X and Liu F 2015 Radial structures of atmospheric-pressure glow discharges with multiple current pulses in helium *J. Phys. D: Appl. Phys.* **48** 345201

[32] Bogaczyk M, Wild R, Stollenwerk L and Wagner H-E 2012 Surface charge accumulation and discharge development in diffuse and filamentary barrier discharges operating in He, N_2 and mixtures *J. Phys. D: Appl. Phys.* **45** 465202

[33] Nemschokmichal S and Meichsner J 2015 Spatio-temporal characterization of $N_2(A^3\Sigma_u^+)$ metastables in diffuse nitrogen barrier discharges *J. Phys. D: Appl. Phys.* **48** 405203

[34] Tschiersch R, Nemschokmichal S, Bogaczyk M and Meichsner J 2017 Surface charge measurements on different dielectrics in diffuse and filamentary barrier discharges *J. Phys. D: Appl. Phys.* **50** 105207

[35] Liu S and Neiger M 2003 Electrical modelling of homogeneous dielectric barrier discharges under an arbitrary excitation voltage *J. Phys. D: Appl. Phys.* **36** 3144

[36] Brandenburg R, Wagner H-E, Morozov A M and Kozlov K V 2005 Axial and radial development of microdischarges of barrier discharges in N_2/O_2 mixtures at atmospheric pressure *J. Phys. D: Appl. Phys.* **38** 1649

[37] Massines F, Rabehi A, Decomps P, Gadri R B, Segur P and Mayoux C 1998 Experimental and theoretical study of a glow discharge at atmospheric pressure controlled by dielectric barrier *J. Appl. Phys.* **83** 2950–7

[38] Golubovskii Y B, Maiorov V A, Behnke J and Behnke J F 2003 Modelling of the homogeneous barrier discharge in helium at atmospheric pressure *J. Phys. D: Appl. Phys.* **36** 39

[39] Obradovic S S, Obradovic B M and Kuraica M M 2008 Spectroscopic measurement of electric field in dielectric barrier discharge in helium *Appl. Phys. Lett.* **92** 191501

[40] Massines F, Gherardi N, Naudé N and Ségur P 2005 Glow and townsend dielectric barrier discharge in various atmosphere *Plasma Phys. Control. Fusion* **47** B577

[41] Lindinger W, Schmeltekopf A L and Fehsenfeld F C 1974 Temperature dependence of de-excitation rate constants of he(23s) by ne, ar, xe, h2, n2, o2, nh3, and co2 *J. Chem. Phys.* **61** 2890–5

[42] Lee F W and Collins C B 1976 Measurement of the rate coefficients for the bimolecular and termolecular de-excitation reactions of he(23s) with ne, ar, n2, co, co2, and ch4 *J. Chem. Phys.* **65** 5189–97

[43] Myers G and Cunningham A J 1977 Quenching reactions of $He(2^3S)$ and $He_2(2^3\Sigma)$ metastables in the presence of N_2 and O_2 *J. Chem. Phys.* **67** 3352–9

[44] Pouvesle J M, Khacef A, Stevefelt J, Jahani H, Gylys V T and Collins C B 1988 Study of two-body and three-body channels for the reaction of metastable helium atoms with selected atomic and molecular species *J. Chem. Phys.* **88** 3061–71

[45] Wild R and Stollenwerk L 2014 Phase-resolved measurement of the spatial surface charge distribution in a laterally patterned barrier discharge *New J. Phys.* **16** 113040